

Neural Born Iterative Method For Solving Inverse Scattering Problems: 2D Cases

Tao Shan, *Member, IEEE*, Zhichao Lin, Xiaoqian Song, Maokun Li, *Senior Member, IEEE*,
Fan Yang, *Fellow, IEEE*, and Shenheng Xu, *Member, IEEE*

Abstract—In this paper, we propose the neural Born iterative method (NeuralBIM) for solving 2D inverse scattering problems (ISPs) by drawing on the scheme of physics-informed supervised residual learning (PhiSRL) to emulate the computing process of the traditional Born iterative method (TBIM). NeuralBIM employs independent convolutional neural networks (CNNs) to learn the alternate update rules of two different candidate solutions regarding the residuals. Two different schemes are presented in this paper, including the supervised and unsupervised learning schemes. With the data set generated by the method of moments (MoM), supervised NeuralBIM are trained with the knowledge of total fields and contrasts. Unsupervised NeuralBIM is guided by the physics-embedded objective function founding on the governing equations of ISPs, which results in no requirement of total fields and contrasts for training. Numerical and experimental results further validate the efficacy of NeuralBIM.

Keywords—Inverse scattering problem, Born iterative method, deep learning, supervised learning, unsupervised learning

I. INTRODUCTION

Inverse scattering are an ubiquitous tool to determine the nature of unknown scatterers with knowledge of scattered electromagnetic (EM) fields [1], which has been applied widely across nondestructive testing [2], biomedical imaging [3], microwave imaging [4], geophysical exploration [5], [6], etc. The intrinsic nonlinearity and ill-posedness pose long-standing challenges to ISPs [1]. Many efforts are devoted to performing reliable inversion by addressing these two challenges, yielding noniterative and iterative inversion methods. Noniterative inversion methods linearize ISPs under specific

This preprint has been published in *IEEE Transactions on Antennas and Propagation* on 01 November 2022. Please cite the final published version as [T. Shan, Z. Lin, X. Song, M. Li, F. Yang and S. Xu, "Neural Born Iterative Method for Solving Inverse Scattering Problems: 2D Cases," in *IEEE Transactions on Antennas and Propagation*, vol. 71, no. 1, pp. 818-829, Jan. 2023, doi: 10.1109/TAP.2022.3217333.]. The link is <https://ieeexplore.ieee.org/document/9934007>.

Digital Object Identifier 10.1109/TAP.2022.3217333

This work was supported in part by the Institute for Precision Medicine, Tsinghua University, in part by the National Natural Science Foundation of China under Grant 61971263 and 62171259, the Biren Technology, the BGP Inc, and the China Postdoctoral Science Foundation under Grant 2022M711764.

Tao Shan, Zhichao Lin, Maokun Li, Fan Yang and Shenheng Xu are with Beijing National Research Center for Information Science and Technology (BNRist), Department of Electronic Engineering, Tsinghua University, Beijing 100084, China. (e-mail: maokunli@tsinghua.edu.cn).

Xiaoqian Song is with National Institute of Metrology, Beijing, 100013, China

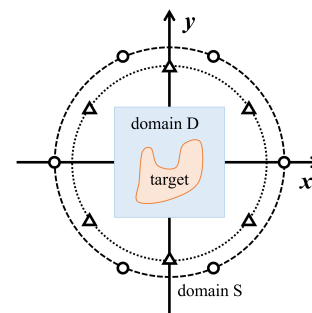


Fig. 1. Model setup of inverse scattering problems. The target is inside the domain D and the triangles and circles represent transmitters and receivers respectively.

conditions, such as Born or Rytov approximation method [7], [8], back-propagation (BP) method [9], etc. Iterative inversion methods transform ISPs into optimization problems of which optimal solutions are identified via an iterative process, for example, Born or distorted Born iterative method [10], [11], contrast source inversion method [12], [13], subspace-based optimization [14], level set method [15], etc. Prior information can be employed as a regularization to constrain and stabilize the iterative method for better inversion performance [16]. Commonly applied regularizations include Tikhonov [17], total variation (TV) [18] and multiplicative regularizations [12]. Besides, the compressive sensing paradigm can introduce an important type of regularization by decomposing the ISP solution based on a set of properly chosen basis functions [19]–[23]. Noniterative inversion methods hold good computational efficiency but limited applicability, while iterative ones can perform reliable inversion but suffer from immense computational loads.

Recently, machine learning (ML), especially deep learning (DL), has been applied in the EM field, such as forward modeling [24]–[26], array antenna design [27]–[29] and ISPs [30], [31], etc., which demonstrates unprecedented numerical precisions and computational efficiency [30]. The supervised descent method (SDM) is trained offline to learn and store the descent directions to guide the online inversions [32]. The powerful learning capacity of deep neural networks (DNNs), like CNNs [33], [34], generative adversarial networks [35], etc., is leveraged to retrieve the properties of scatterers from the scattered fields directly. Moreover, the combination of DL and traditional ISP methods can achieve improved computational efficiency and inversion quality [30]. DNNs are

trained to enhance the initial guess of inversions generated by noniterative inversion methods [36]–[38]. Conversely, iterative inversion methods can take as input the reconstructions predicted by DNNs [39], [40]. Despite the remarkable success, most of the works mentioned above regard DNNs as "black-box" approximators, and the challenge of designing DNNs effective for ISPs has not been fully addressed.

The ordinary or partial differential equations (ODEs/PDEs) theory enables better insights into DNN properties, which guides the design of effective DNN architectures with better robustness and interpretability. In [41], ResNet, PolyNet, FractalNet, and RevNet are linked to different numerical methods of ODEs or PDEs, respectively. ResNet can also be interpreted from the perspective of dynamical systems [42], [43] or combined with the fixed-point iterative method [44]. The spectral method and random matrix theory are combined to weigh the trainability of DNN architectures by analyzing their dynamical isometry [45], [46]. PDE-Net is proposed based on the similarities between finite difference operators and convolution operations [47]. New structures of ResNets for image processing are motivated by parabolic, and hyperbolic PDEs [48].

In this paper, we propose the neural Born iterative method by drawing on PhiSRL to emulate the computational process of the traditional Born iterative method. Combining ResNet [49] and the fixed-point iterative method, PhiSRL iteratively modifies a candidate solution until convergence by applying CNNs to predict the modification. NeuralBIM builds the learned parameterized functions for the alternate update process of TBIM by drawing on the idea of PhiSRL. Therefore, NeuralBIM bears the same computation as TBIM to reconstruct the total fields and scatterers simultaneously. The supervised and unsupervised learning schemes of NeuralBIM are demonstrated and validated in this paper. Supervised NeuralBIM is first presented to be trained by applying MoM to generate total fields and contrasts as labels. Unsupervised NeuralBIM is proposed by deriving the physics-embedded objective function from the governing equations of ISPs, which further gets rid of total fields and contrasts for training. Numerical and experimental results verify the efficacy of NeuralBIM.

This paper is organized as follows. Section II formulates inverse scattering problems. Section III introduces traditional Born iterative method. Both supervised and unsupervised neural Born iterative methods are introduced in Section IV. Section V demonstrates the numerical and experimental results of neural Born iterative method. Finally, Section VI draws conclusions and outlooks.

II. INVERSE SCATTERING PROBLEMS

In a 2D domain of interest (DoI) D , the transverse magnetic (TM) polarized line sources illuminate the unknown scatterers. The incident field E^i , total field E^t and scattered field E^s are related by

$$E^t(\mathbf{r}) = E^i(\mathbf{r}) + k_b^2 \int_D G_D(\mathbf{r}, \mathbf{r}') \chi(\mathbf{r}') E^t(\mathbf{r}') d\mathbf{r}', \mathbf{r} \in D \quad (1)$$

$$E^s(\mathbf{r}'') = \int_D G_S(\mathbf{r}'', \mathbf{r}') \chi(\mathbf{r}') E^t(\mathbf{r}') d\mathbf{r}', \mathbf{r}'' \in S \quad (2)$$

where k_b is the wavenumber, G_D and G_S denote Green's functions in free space, $\chi(\mathbf{r})$ is the scatterer contrast and S is the observation domain. Eq. (1) and Eq. (2) can be discretized into a linear system of matrix equations by employing MoM:

$$(\mathbf{I} - \mathbf{G}_D \chi) \mathbf{E}^t = \mathbf{E}^i \quad (3)$$

$$\mathbf{E}^s = \mathbf{G}_S \chi \mathbf{E}^t \quad (4)$$

ISPs aims to reconstruct χ based on the governing equations (Eq. (3) and Eq. (4)).

III. TRADITIONAL BORN ITERATIVE METHOD

Traditional Born iterative method is one of the effective algorithms for solving ISPs [7]. TBIM reconstructs unknown scatterers with the knowledge of incident and scattered fields via an alternate update process. TBIM first establishes the following minimization problem:

$$\min_{\chi} \|\mathbf{E}^s - \mathbf{G}_S \chi \mathbf{E}^t\|^2. \quad (5)$$

The optimal solution χ_{next} of Eq. (5) serves as the update of χ .

Then, the total field \mathbf{E}^t can be updated with χ_{next} :

$$\mathbf{E}_{next}^t = (\mathbf{I} - \mathbf{G}_D \chi_{next})^{-1} \mathbf{E}^i \quad (6)$$

In TBIM, Eq. (5) and Eq. (6) are applied alternatively in the iterative process until \mathbf{E}^t and χ satisfy the stop criterion. In the first update of χ , the incident field \mathbf{E}^i is used to approximate the total field \mathbf{E}^t in Eq. (5). Here, Eq. (5) is viewed and solved as a least-square problem as stated in [10], [11]. Eq. (6) is solved directly by MoM where the computation of \mathbf{G}_D is accelerated by fast Fourier transform. The algorithm flow of TBIM is summarized in Algorithm 1.

Algorithm 1 Traditional Born Iterative Method

Initialization: $\mathbf{E}_0^t = \mathbf{E}^i$, $k = 0$, $stopflag = 1$
while $stopflag$ **do**
 step 1: $\chi_{k+1} = \arg \min_{\chi} \|\mathbf{E}^s - \mathbf{G}_S \chi \mathbf{E}_k^t\|^2$
 step 2: $\mathbf{E}_{k+1}^t = (\mathbf{I} - \mathbf{G}_D \chi_{k+1})^{-1} \cdot \mathbf{E}^i$
 step 3: $k = k + 1$
 if stop criteria is satisfied **then**
 $stopflag = 0$
 end if
end while
output: χ_k, \mathbf{E}_k^t

IV. NEURAL BORN ITERATIVE METHOD

Neural Born iterative method is motivated by the physics-informed supervised residual learning. PhiSRL is built by interpreting ResNet as the fixed-point iterative method [44]. PhiSRL aims to solve the matrix equation $\mathbf{A}\mathbf{x} = \mathbf{b}$ and its $k + 1$ -th update equation can be formulated as:

$$\mathbf{x}_{k+1} = \mathbf{x}_k + \mathcal{F}_{k+1}(\mathbf{R}_k, \Theta_{k+1}), \quad (7)$$

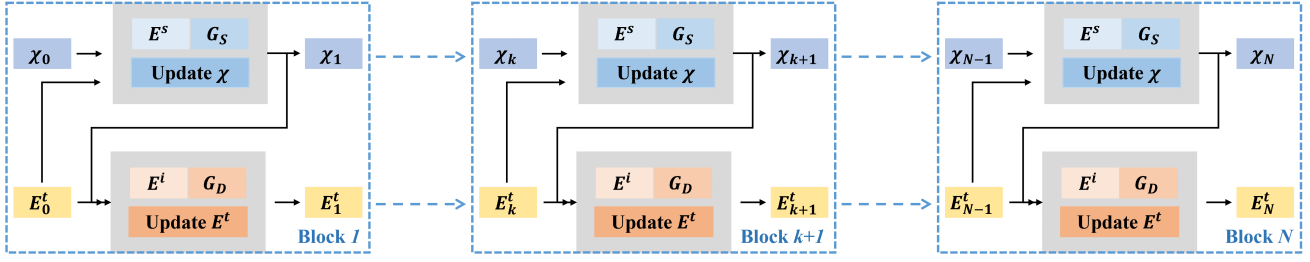


Fig. 2. The architecture of Neural Born iterative method. NeuralBIM is assumed to have 7 blocks in this paper with Block k denoting the k -th iteration. The contrast χ is first updated and then employed to update the total field \mathbf{E}^t in the k -th iteration.

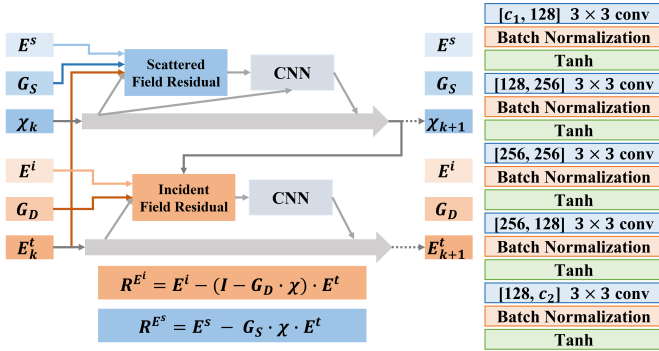


Fig. 3. The iterative block of Neural Born iterative method. $\mathcal{R}_k^{\mathbf{E}^s}$ and $\mathcal{R}_k^{\mathbf{E}^i}$ represent the incident and scattered field residuals. χ_{k+1} is updated by χ -CNN based on $\mathcal{R}_k^{\mathbf{E}^s}$ and χ_k . Then $\mathcal{R}_k^{\mathbf{E}^i}$ is obtained regarding χ_{k+1} and then input to \mathbf{E}^t -CNN to update \mathbf{E}_{k+1}^t . The χ -CNN and \mathbf{E}^t -CNN share the same architecture but different parameter sets.

where \mathcal{F}_{k+1} and Θ_{k+1} denote the CNN and corresponding parameter set, $\mathbf{R}_k = \mathbf{b} - \mathbf{A}\mathbf{x}_k$ denotes the residual of k -th iteration. It can be observed from Eq. (7) that PhiSRL applies CNNs to iteratively update the candidate solutions regarding the calculated residuals, which further motivates the application of PhiSRL to emulate the computing process of TBIM.

NeuralBIM are designed by applying CNNs to alternatively update both total fields and contrasts in TBIM. The difference between TBIM and NeuralBIM lies in that NeuralBIM applies CNNs to learn the update rules instead of the hand-crafted rules (Eq. (5) and Eq. (6)). Combining Eq. (5) and Eq. (7), the update of χ can be written as:

$$\begin{aligned} \mathcal{R}_k^{\mathbf{E}^s} &= \mathbf{E}^s - \mathbf{G}_S \chi_k \mathbf{E}_k^t, \\ \chi_{k+1} &= \chi_k + \mathcal{F}_{k+1}^\chi(\mathcal{R}_k^{\mathbf{E}^s} \oplus \chi_k, \Theta_{k+1}^\chi), \end{aligned} \quad (8)$$

where $\mathcal{R}_k^{\mathbf{E}^s}$ represents the residual of scattered field, \mathcal{F}_{k+1}^χ and Θ_{k+1}^χ denote the χ -CNN and corresponding parameter set, \oplus is the concatenation of two tensors. It is worth noting that the input of the χ -CNN adopts the concatenation of the calculated residual and the previous contrast. This is because \mathbf{G}_S in Eq. (4) reduces the dimensionality of total fields and results in the loss of information. Taking χ as another input of the χ -CNN can enable better performance of inversions according to the authors' trials. Similarly, the update of total

field \mathbf{E}^t can be formulated by combining Eq. (6) and Eq. (7):

$$\begin{aligned} \mathcal{R}_k^{\mathbf{E}^i} &= \mathbf{E}^i - (\mathbf{I} - \mathbf{G}_D \chi_{k+1}) \mathbf{E}_k^t, \\ \mathbf{E}_{k+1}^t &= \mathbf{E}_k^t + \mathcal{F}_{k+1}^{\mathbf{E}^t}(\mathcal{R}_k^{\mathbf{E}^i}, \Theta_{k+1}^{\mathbf{E}^t}), \end{aligned} \quad (9)$$

where $\mathcal{R}_k^{\mathbf{E}^i}$ is the residual of the incident field, $\mathcal{F}_{k+1}^{\mathbf{E}^t}$ and $\Theta_{k+1}^{\mathbf{E}^t}$ are the \mathbf{E}^t -CNN and corresponding parameter set. The algorithm flow of NeuralBIM is summarized in Algorithm 2.

Algorithm 2 Neural Born Iterative Method

initialization: $\mathbf{E}_0^{tot} = \mathbf{E}^{inc}$, $\chi_0 = 0$, $k = 0$, $MaxIter$
while $k < MaxIter$ **do**
 step 1: $\mathcal{R}_k^{\mathbf{E}^s} = \mathbf{E}^s - \mathbf{G}_S \chi_k \mathbf{E}_k^t$
 step 2: $\chi_{k+1} = \chi_k + \mathcal{F}_{k+1}^\chi(\mathcal{R}_k^{\mathbf{E}^s} \oplus \chi_k, \Theta_{k+1}^\chi)$
 step 3: $\mathcal{R}_k^{\mathbf{E}^i} = \mathbf{E}^i - (\mathbf{I} - \mathbf{G}_D \chi_{k+1}) \mathbf{E}_k^t$
 step 4: $\mathbf{E}_{k+1}^t = \mathbf{E}_k^t + \mathcal{F}_{k+1}^{\mathbf{E}^t}(\mathcal{R}_k^{\mathbf{E}^i}, \Theta_{k+1}^{\mathbf{E}^t})$
 step 5: $k = k + 1$
end while
output: $\chi_{MaxIter}$, $\mathbf{E}_{MaxIter}^t$

In this paper, NeuralBIM is assumed to have 7 iterative modules as depicted in Figure 2. Figure 3 illustrates the detailed structure of the iterative block. The χ -CNN and \mathbf{E}^t -CNN to modify contrasts and total fields share the same structure but different parameter sets. The employed CNN comprises five stacked operations including 3×3 convolution, batch normalization and Tanh nonlinearity, as shown in Figure 3. Tanh nonlinearity can provide both positive and negative values, which allows an adaptive modification of the candidate solution. The input and output channels are also denoted in the Figure 3. The c_1 and c_2 are 4 and 2 for updating lossy contrasts, and 2 and 2 for updating the total fields.

The training schemes of NeuralBIM include the supervised and unsupervised learning schemes:

Supervised learning scheme: The supervised learning scheme trains the NeuralBIM with the total fields and contrasts as labels. The objective function is defined as:

$$obj_{su} = loss_{\mathbf{E}^t} + loss_\chi, \quad (10)$$

where $loss_{\mathbf{E}^t}$ and $loss_\chi$ denote the losses of total fields and contrasts respectively. The $loss_{\mathbf{E}^t}$ is defined as the mean squared error (MSE):

$$loss_{\mathbf{E}^t} = \frac{1}{N_{\mathbf{E}^t}} \|\mathbf{E}^{t*} - \mathbf{E}^t\|_F^2, \quad (11)$$

where \mathbf{E}^{t*} and $\mathbf{E}^{t'}$ denote the ground-truth and predicted total field, $N_{\mathbf{E}^{t'}}$ denotes the element number in the vector of $\mathbf{E}^{t'}$, $\|\cdot\|_F$ represents Frobenius norm. The $loss_{\chi}$ adds the TV regularization item to the MSE of contrasts:

$$loss_{\chi} = \frac{1}{N_{\chi'}} \|\chi^* - \chi'\|_F^2 + \alpha \frac{1}{N_{\chi'}} \|\nabla \chi'\|_1, \quad (12)$$

where χ^* and χ' are the ground-truth and inverted contrast, $N_{\chi'}$ denotes the element number in the vector of χ' , $\|\cdot\|_1$ is L1 norm, α is fixed as 0.0001. In the supervised training scheme, NeuralBIM is trained to generate accurate predictions of total fields and contrasts. It takes a certain amount of time to generate training data samples by applying MoM to solve Eq. (3) and Eq. (4). This scheme is also different from the practical applications where total fields and contrasts are unknown.

Unsupervised learning scheme: In the unsupervised learning scheme, total fields and contrasts are unknown when training NeuralBIM. The training of NeuralBIM is constrained and guided by the governing equations of ISPs as formulated in Eq. (3) and Eq. (4). The objective function is defined as:

$$obj_{unsu} = res_{\mathbf{E}^i} + res_{\mathbf{E}^s}, \quad (13)$$

The $res_{\mathbf{E}^i}$ is formulated based on Eq. (3):

$$res_{\mathbf{E}^i} = \frac{1}{N_{\mathbf{E}^i}} \|(\mathbf{I} - \mathbf{G}_D \chi') \mathbf{E}^{t'} - \mathbf{E}^i\|_F^2. \quad (14)$$

The $res_{\mathbf{E}^s}$ is defined based on Eq. (4):

$$res_{\mathbf{E}^s} = \frac{1}{N_{\mathbf{E}^s}} \|\mathbf{E}^s - \mathbf{G}_S \chi' \mathbf{E}^{t'}\|_F^2 + \alpha \frac{1}{N_{\chi'}} \|\nabla \chi'\|_1, \quad (15)$$

where $N_{\mathbf{E}^i}$ and $N_{\mathbf{E}^s}$ denote the element number in the vector of \mathbf{E}^i and \mathbf{E}^s , $\|\nabla \chi'\|_1$ is the TV regularization and α is fixed as 0.0001. It is noted that the incident and scattered fields in Eq. (14) and Eq. (15) are assumed to be known in ISPs and the Green functions are determined by the measurement setup of ISPs. The unsupervised training scheme aims to train NeuralBIM to generate solutions simultaneously satisfying Eq. (3) and Eq. (4) by leveraging the existing physical law and information. The TV regularization can stabilize the training process by enforcing the boundaries of reconstructions.

The computational complexity of NeuralBIM is determined by two parts: the matrix multiplication in calculating residuals and the basic computation in the CNN. In a single iteration, NeuralBIM has two subsequent branches to update χ and \mathbf{E}^t respectively. The numbers of transmitters, receivers and pixels are denoted as T , R and P for simplification. In the χ -branch, the complexity of calculating $\mathcal{R}^{\mathbf{E}^s}$ is $O(TRP)$ due to the dense matrix multiplication. The complexity of the χ -CNN is dominated by convolution operations. For a single convolutional layer, the complexity is $O(PK^w K^h C_{\chi}^i C_{\chi}^o)$, where K^w and K^h are the width and height of the convolutional kernel, C_{χ}^i and C_{χ}^o are the input and output channels. Assuming the χ -CNN has L layers, its complexity can be written as: $O(\sum_{l=1}^L PK_l^w K_l^h C_{\chi,l}^i C_{\chi,l}^o)$. Note that all feature maps output by the convolutional layers contain P pixels. Similarly, in the \mathbf{E}^t -branch, the complexity of the calculation of $\mathcal{R}_k^{\mathbf{E}^t}$ and the \mathbf{E}^t -CNN are $O(TP^2)$ and

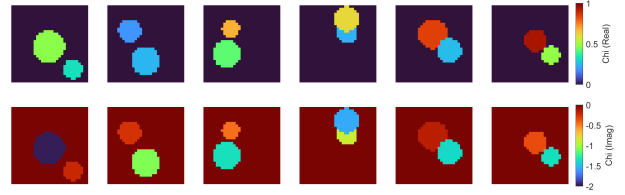


Fig. 4. Examples of scatterers in the synthetic data set. Two cylinders have random locations and radii, as detailed in Table I.

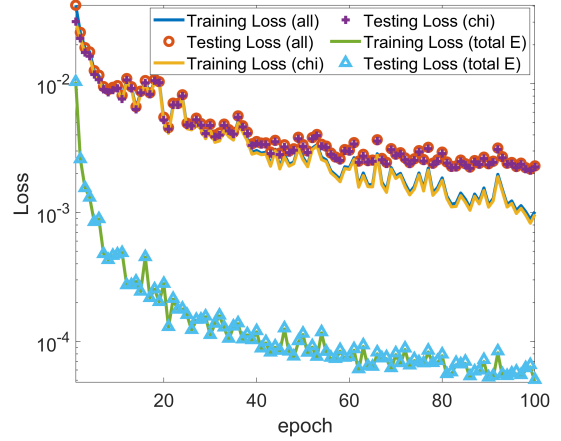


Fig. 5. Convergence curve of supervised NeuralBIM. Training and testing loss (all, chi, total E) denote obj_{su} , $loss_{\chi}$, and $loss_{\mathbf{E}^t}$.

$O(\sum_{l=1}^L PK_l^w K_l^h C_{\mathbf{E}^t,l}^i C_{\mathbf{E}^t,l}^o)$ respectively. The complexity of calculating $\mathcal{R}_k^{\mathbf{E}^t}$ can be further reduced by fast Fourier transform in the case of large-scale problems. For NeuralBIM with N iterations, the total computational complexity is $O(NTRP + N \sum_{l=1}^L PK_l^w K_l^h C_{\chi,l}^i C_{\chi,l}^o + NTP^2 + N \sum_{l=1}^L PK_l^w K_l^h C_{\mathbf{E}^t,l}^i C_{\mathbf{E}^t,l}^o)$.

V. NUMERICAL RESULTS

In this section, we first validate both supervised and unsupervised NeuralBIM with synthetic data inversion. The efficacy of unsupervised NeuralBIM is further verified with experimental data inversion. Supervised and unsupervised NeuralBIM are implemented in Pytorch and computed on three Nvidia V100 GPUs. The Adam optimizer is adopted to train NeuralBIM. The learning rate is initialized as 0.002 and decayed by $\sim \times 0.8$ every 20 epochs.

TABLE I
TRAINING SETTINGS IN SYNTHETIC DATA INVERSION

Cylinder	Radius	Contrast (Real)	Contrast (Imag)
A	0.015-0.035m	[0, 1]	[-1, 0]
B	0.015-0.035m	[0, 1]	[-2, -1]

A. Synthetic Data Inversion

As depicted in Figure 1, D has a size of $0.15m \times 0.15m$ and it is uniformly discretized into 32×32 grids. 32 transmitters and receivers are evenly distributed on a circle outside D of which radius is $1.67m$. The incident frequency is 3GHz. Two cylinders are randomly located inside D as summarized in

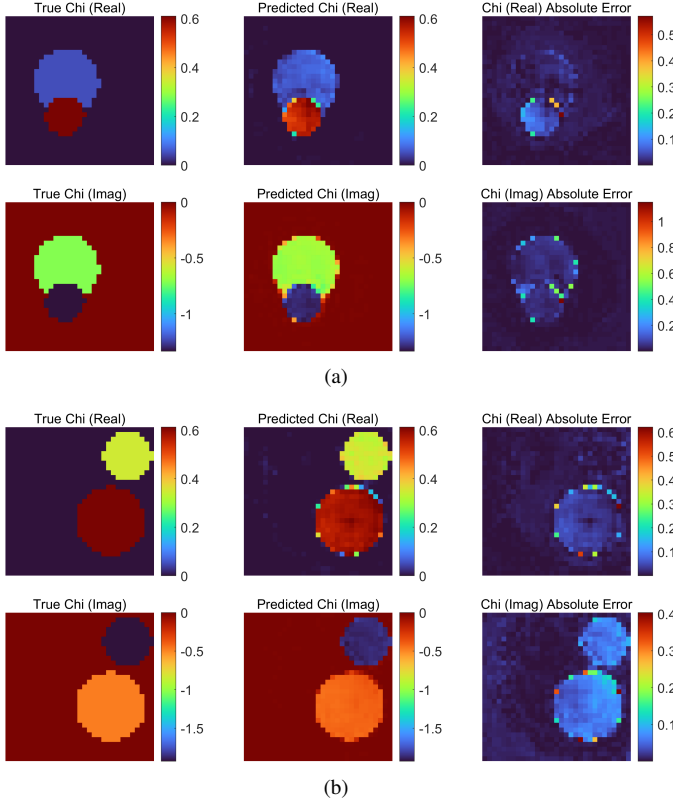


Fig. 6. Comparison between ground truth and scatterers inverted by supervised NeuralBIM. From left to right are: ground truth, reconstruction and their absolute error distribution.

Table I. Figure 4 shows several examples of scatterer shapes. The data set is generated by MoM. Supervised and unsupervised NeuralBIM are trained and tested on the same data set. The data set comprises 20000 data samples of which 80% are for training and 20% for testing. The initial guess of the total field adopts the incident field. BP method is applied to generate the initial guess of the contrast.

1) *Supervised Neural Born Iterative Method*: Figure 5 plots the convergence curves of obj_{su} , $loss_{E^t}$ and $loss_{\chi}$. All of them drop steadily as the training progresses. It can be observed that $loss_{\chi}$ dominates $loss_{E^t}$ with the small value of $loss_{E^t}$. The testing $loss_{\chi}$ is a little higher than the training one which leads to overfitting. The overfitting can be alleviated by introducing better regularizations or stopping training earlier.

Figure 6 depicts the comparisons between ground truth and reconstructions that are randomly chosen in the testing data set. The inverted contrasts are in a good agreement with the ground truth as reflected in the absolute error distributions. The differences mostly lie on the boundaries of scatterer shapes.

The updated reconstructions of contrasts are illustrated in Figure 7. The update of contrast begins with the initial guess generated by BP method and it improves gradually with the increase of iterations.

The mean absolute error (MAE) histograms of all data samples are charted in Figure 8(a). The specific means and standard deviations (stds) are summarized in Table II. The MAE histogram of total fields has small means and stds, and this indicates the good reconstruction precisions. The MAE

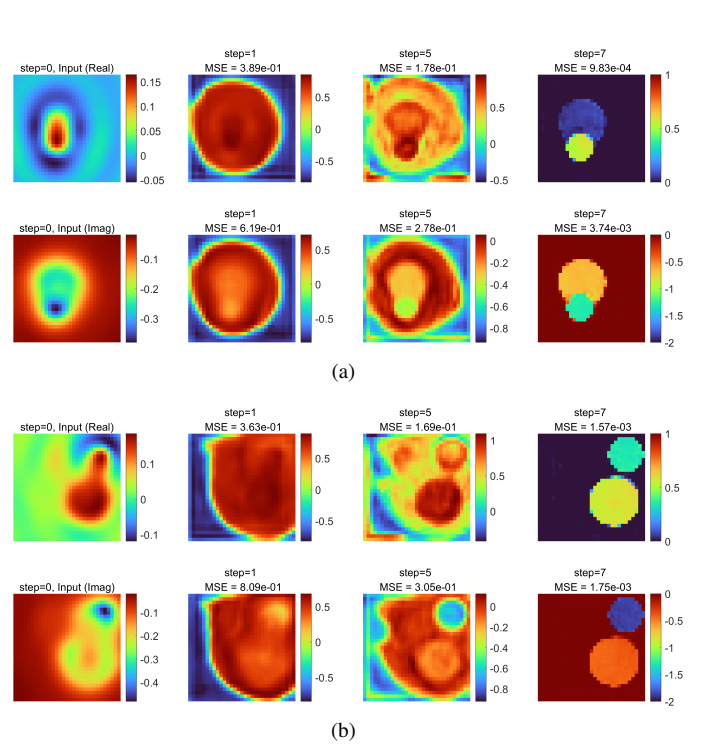


Fig. 7. Updated reconstructions of contrasts in the iterative computing of supervised NeuralBIM. From left to right are: initial guess, reconstructions at the first, fifth and seventh iteration. In each sub-panel, the first and second row show the real and imaginary parts.

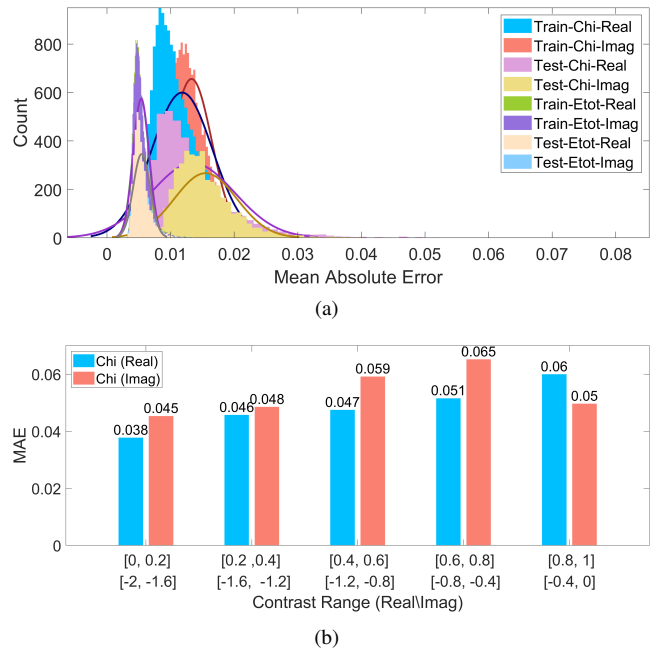


Fig. 8. MAE histograms of contrasts and total fields inverted by supervised NeuralBIM. (a) is a histogram of the reconstruction MAE of each data sample in training and testing data sets. (b) is a histogram of the reconstruction MAE of each cylinder for different contrast ranges for all data samples. Chi, Etot, Real, Imag denote the contrast, total field, real part and imaginary part in the legend.

TABLE II
MAE MEANS AND STANDARD DEVIATIONS OF SUPERVISED NEURALBIM

Item	MAE-R* (mean/std)	MAE-I† (mean/std)
Contrast (train) ¹	0.0118/0.0048	0.0133/0.0032
Contrast (test) ²	0.0135/0.0066	0.0155/0.0049
Total field (train) ³	0.0054/0.0013	0.0053/0.0012
Total field (test) ⁴	0.0055/0.0013	0.0054/0.0013

¹ contrasts in training data set
² contrasts in testing data set
³ total fields in training data set
⁴ total fields in testing data set
 * MAE of real part
 † MAE of imaginary part



Fig. 9. The final losses of supervised NeuralBIM trained with data sets of different sizes. Training and testing loss (all, chi, total E) denote obj_{su} , $loss_{\chi}$, and $loss_{\mathbf{E}}$.

histogram of testing contrasts has higher mean and std than the one of training contrasts, which is consistent with the convergence curve in the Figure 5. Figure 8(b) charts a histogram of the reconstruction MAE of each cylinder at different contrast ranges for all data samples. The reconstruction MAE is only evaluated for the cylinders and the background is not considered. The real and imaginary part ranges of the contrast is evenly divided into five intervals respectively. For real parts, the five intervals are $[0, 0.2]$, $[0.2, 0.4]$, $[0.4, 0.6]$, $[0.6, 0.8]$, $[0.8, 1.0]$, and they are $[-2, -1.6]$, $[-1.6, -1.2]$, $[-1.2, -0.8]$, $[-0.8, -0.4]$, $[-0.4, 0]$ for imaginary parts. Supervised NeuralBIM shows a stable performance regarding a wide range of contrast values.

The impact of data set sizes on the performance of supervised NeuralBIM is first investigated. The data sets are assumed to have 5000, 10000, 15000, 20000 samples respectively, of which 80% and 20% are for training and testing. For all data sets, all training processes are assumed to stop at the 100th epoch. Figure 9 shows the final losses of supervised NeuralBIM trained with data sets of different sizes. It can be observed that the larger the training data set, the better the reconstruction performance. When the size of data set increases from 15000 to 20000, the testing $loss_{\chi}$ is slightly reduced although the training $loss_{\chi}$ has a noticeable drop. Therefore, considering the training time, the data set of 20000 samples is adopted to train NeuralBIM in this paper.

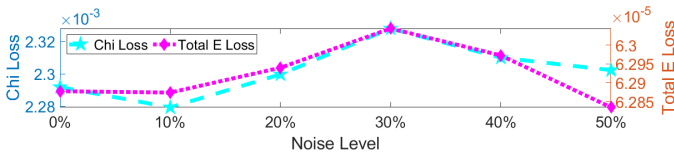


Fig. 10. Losses of contrasts and total fields reconstructed by supervised NeuralBIM under different noise levels. Chi and total E denote contrast and total field.

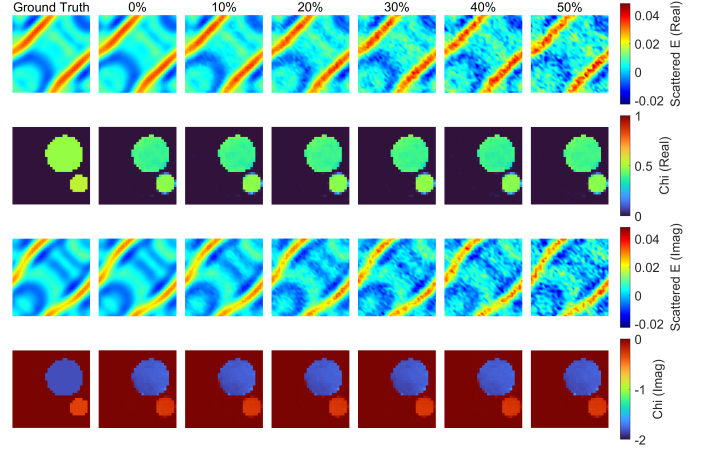


Fig. 11. Reconstructed scatterers of supervised NeuralBIM under different noise levels. From left to right are ground truth, reconstructions at the noise level of 0%, 10%, 20%, 30%, 40%, 50%.



Fig. 12. Verification of generalization ability of supervised NeuralBIM on different scatterer shapes.

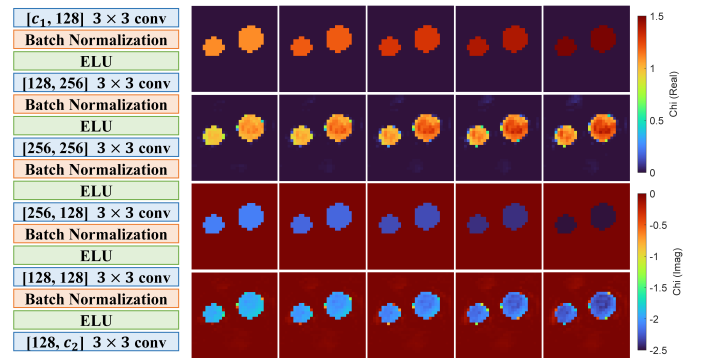


Fig. 13. The CNN structure and the reconstructed scatterers in different contrasts. The CNN structure in the re-trained supervised NeuralBIM (left sub-panel) and the reconstructed scatterers in different contrasts (right sub-panel). From left to right, the contrasts are: $1.1 - j2.1$, $1.2 - j2.2$, $1.3 - j2.3$, $1.4 - j2.4$, $1.5 - j2.5$.

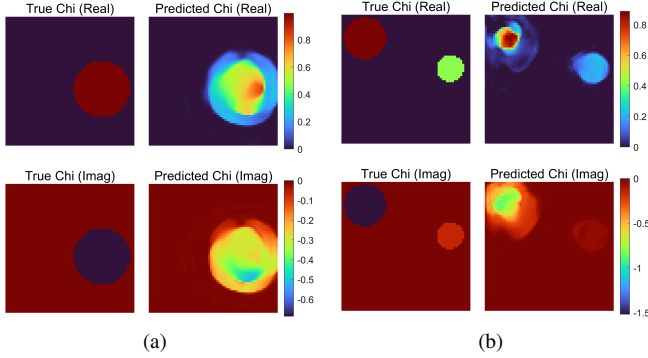


Fig. 14. Reconstructions of 64×64 grids. (a): one cylinder, (b): two cylinders. In each sub-panel, from left to right are: ground truth and the reconstructed scatterers.

The anti-noise capability is then validated. We randomly select 20 testing data samples and add different levels of Gaussian white noise. Figure 10 plots $loss_{\mathbf{E}^t}$ and $loss_{\chi}$ of each noise level. Both $loss_{\mathbf{E}^t}$ and $loss_{\chi}$ fluctuate within a very small range, which demonstrates the strong anti-noise capability of supervised NeuralBIM. The inverted contrasts are detailed in Figure 11. The reconstruction maintains a good and stable quality even at the noise level of 50%.

The generalization ability is also verified on different scatterer geometries unseen at the training time. Six different kinds of scatterer geometries are considered as shown in Figure 12. The comparisons between the ground truth and reconstructions are demonstrated in Figure 12. Supervised NeuralBIM can perform reliable inversion although the scatterer geometries are not included in the training data set. The discrepancy primarily lies in the tiny structures that are hard to distinguish.

Furthermore, supervised NeuralBIM is employed to invert the scatterers with higher contrasts. Supervised NeuralBIM with CNN structures as shown in Figure 3 is insensitive to the higher contrasts, which could be caused by that Tanh functions are saturating nonlinearities. The modified CNN model with ELU nonlinearities [50] is adopted as shown in Figure 13. The modified supervised NeuralBIM is re-trained under the same training settings. It demonstrates an improved performance on inverting scatterers on higher contrasts, as shown in Figure 13.

Supervised NeuralBIM is also tested whether it can be generalized to solve large-scale problems when trained for small-scale problems. Supervised NeuralBIM is trained on 32×32 grids. Then, it is applied to perform inversion of 64×64 grids. According to Eq. (8), in the k -th iteration, χ -CNN is dependent on the concatenation of $\mathcal{R}_k^{\mathbf{E}^s}$ and χ_k . Note that $\mathcal{R}_k^{\mathbf{E}^s}$ and χ_k have the same size and are concatenated in the channel dimension. The size of $\mathcal{R}_k^{\mathbf{E}^s}$ is determined by the number of transmitters and receivers. When the size of χ_k is 64×64 , the number of transmitters and receivers need be set as 64. Such change of the measurement configuration results in a reduced reconstruction performance of Supervised NeuralBIM. Figure 14 demonstrates two different reconstructed scatterers of 64×64 grids. The inverted results can reflect the locations and shapes of scatterers but the corresponding contrast values are not accurate enough.

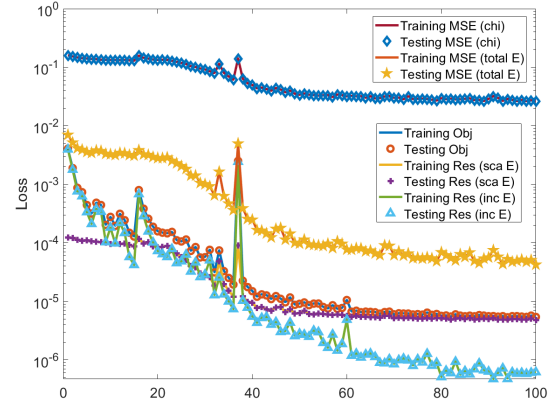


Fig. 15. Convergence curve of unsupervised NeuralBIM. Training and testing Obj denote the curves of obj_{su} . Training and testing Res (sca E, inc E) denote the curves of $res_{\mathbf{E}^s}$, and $res_{\mathbf{E}^i}$. Training and testing MSE (chi, total E) denote the curves of $eval_{\chi}$, and $eval_{\mathbf{E}^t}$.

2) *Unsupervised Neural Born Iterative Method*: The convergence curves of unsupervised NeuralBIM are summarized in Figure 15. It is shown that obj_{unsu} , $res_{\mathbf{E}^i}$ and $res_{\mathbf{E}^s}$ fall steadily as the training progresses. They fluctuate several times due to the unsupervised learning scheme. Since $res_{\mathbf{E}^i}$ and $res_{\mathbf{E}^t}$ cannot reflect the performance intuitively, the MSEs between the ground truth and the reconstructions are employed as the evaluation functions:

$$\begin{aligned} eval_{\mathbf{E}^t} &= \frac{1}{N_{\mathbf{E}^t}} \|\mathbf{E}^{t*} - \mathbf{E}^{t'}\|_F^2 \\ eval_{\chi} &= \frac{1}{N_{\chi}} \|\chi^* - \chi'\|_F^2. \end{aligned} \quad (16)$$

The convergence curves of $eval_{\mathbf{E}^t}$ and $eval_{\chi}$ are also plotted in Figure 15. The curves of $eval_{\mathbf{E}^t}$ and $eval_{\chi}$ have the same trends as the ones of obj_{unsu} , which further validates the efficacy of the objective function based on the governing equations (Eq. (3) and Eq. (4)).

Figure 16 demonstrates two reconstructed contrasts that are randomly chosen in the testing data set. The inverted contrasts are in good agreement with the ground truth, and the absolute error distributions are in a low error level. The TV regularization enables the homogenous background and the boundaries of scatterers in the reconstructions.

Figure 17 demonstrates the updated reconstructions of contrasts during the alternate update process. The initial guesses of contrasts are generated by BP method. The candidate contrasts are continuously modified with the increase of iterations.

Figure 18(a) charts the MAE histograms of inverted contrasts and total fields in the training and testing data sets. The specific means and stds of MAE histograms are summarized in Table III. The real parts of inverted scatterers have better precisions than the imaginary parts. The MAE histograms of training and testing data have close means and stds, which is consistent with the convergence curve shown in Figure 15. Figure 18(b) plots the reconstruction MAE of each cylinder at different contrast ranges for all data samples. The contrast range is divided in the same way as Figure 8(b). It can be observed that the MAEs grow with the increase of absolute values of contrasts. In order to improve the performance on

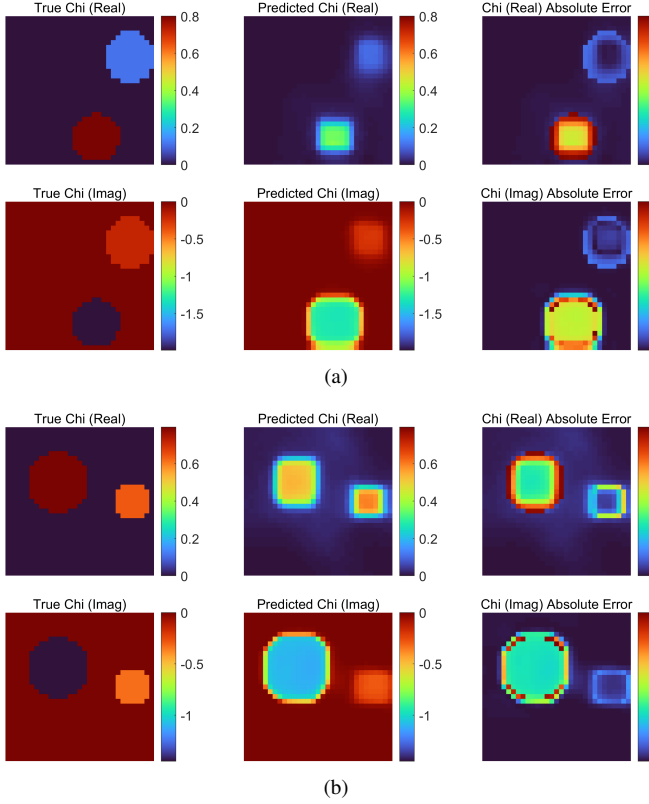


Fig. 16. Comparison between ground truth and scatterers inverted by unsupervised NeuralBIM. From left to right are: ground truth, reconstruction and their absolute error distribution.

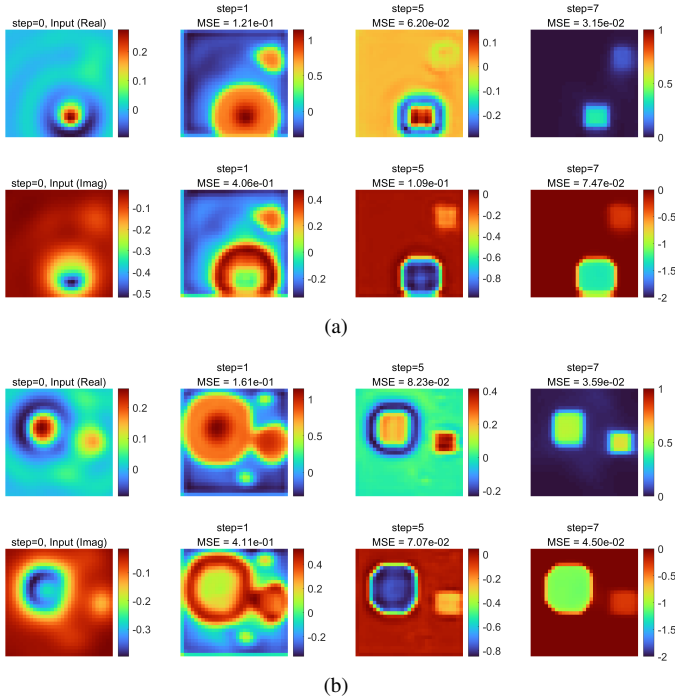


Fig. 17. Updated reconstructions of contrasts in the iterative computing of unsupervised NeuralBIM. From left to right are: initial guess, reconstructions at the first, fifth and seventh iteration. In each sub-panel, the first and second row show the real and imaginary parts.

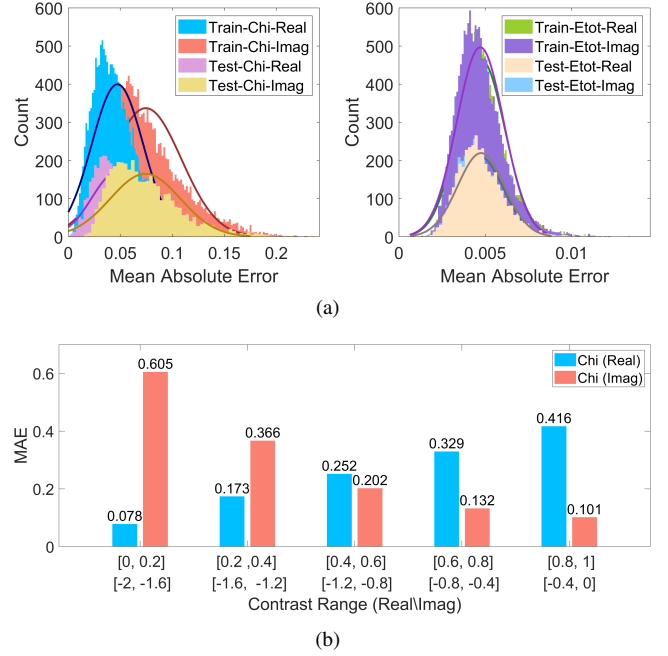


Fig. 18. MAE histograms of contrasts and total fields inverted by unsupervised NeuralBIM. (a) is a histogram of the reconstruction MAE of each data sample in training and testing data sets. (b) is a histogram of the reconstruction MAE of each cylinder at different contrast ranges for all data samples. Chi, Etot, Real, Imag denote the contrast, total field, real part and imaginary part in the legend.

TABLE III
MAE MEANS AND STANDARD DEVIATIONS OF UNSUPERVISED NEURALBIM

Item	MAE-R* (mean/std)	MAE-I+ (mean/std)
Contrast (train) ¹	0.0472/0.0248	0.0745/0.0341
Contrast (test) ²	0.0465/0.0239	0.0740/0.0337
Total field (train) ³	0.0047/0.0014	0.0048/0.0014
Total field (test) ⁴	0.0047/0.0013	0.0048/0.0014

¹ contrasts in training data set

² contrasts in testing data set

³ total fields in training data set

⁴ total fields in testing data set

* MAE of real part

+ MAE of imaginary part

the cases of high contrasts, we can increase the proportion of high contrast samples in the training data set.

The performance of unsupervised NeuralBIM is then evaluated under different noise levels of scattered fields. A total of 20 data samples are selected from the testing data set and the Gaussian white noise is added to the field data for validation. The curves of $eval_{E_t}$ and $eval_{\chi}$ are plotted in Figure 19. It can be observed that both $eval_{E_t}$ and $eval_{\chi}$ are

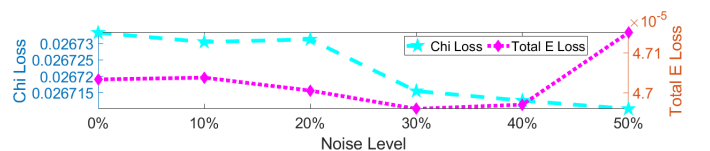


Fig. 19. Losses of contrasts and total fields reconstructed by unsupervised NeuralBIM under different noise levels. Chi and total E denote contrast and total field.

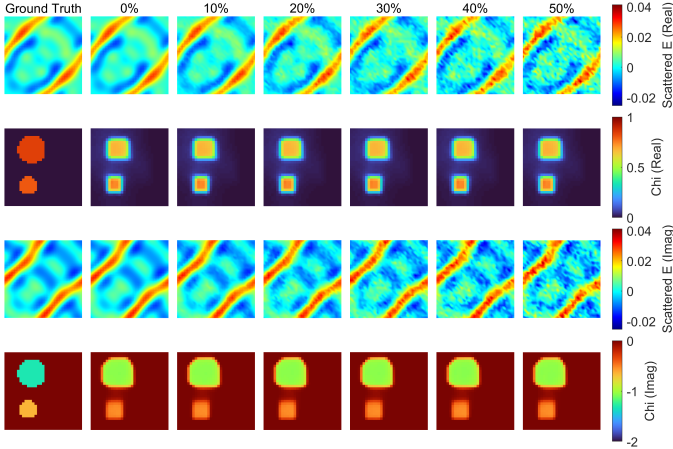


Fig. 20. Reconstructed scatterers of unsupervised NeuralBIM under different noise levels. From left to right are ground truth, reconstructions at the noise level of 0%, 10%, 20%, 30%, 40%, 50%.



Fig. 21. Verification of generalization ability of unsupervised NeuralBIM on different scatterer shapes.

stable under different noise levels. The anti-noise capability of unsupervised NeuralBIM is verified. The inverted scatterers at the noise level from 0% to 50% are compared in Figure 20. The inverted scatterers demonstrates a good and stable image quality.

The generalization ability on scatterer shapes is then verified. The shapes of scatterers are totally different from the training ones. The corresponding reconstructions are demonstrated in Figure 21. The inverted scatterers are in good agreement with the ground truth with clear boundaries.

B. Comparison With TBIM

The performances of TBIM, supervised and unsupervised NeuralBIM are compared in this section. NeuralBIM is assumed to stop at the 7-th iteration and TBIM converges at the 14-th iteration. The TBIM is computed on Intel(R) Core(TM) i5-9600K CPU @ 3.70GHz. Besides, the initial guess of TBIM is also generated by BP method. The testing example assumes that three cylinders are located in D . The real and imaginary parts of their contrasts are in $[0, 1]$ and $[-2, 0]$ respectively. Note that the testing example is unseen during the training

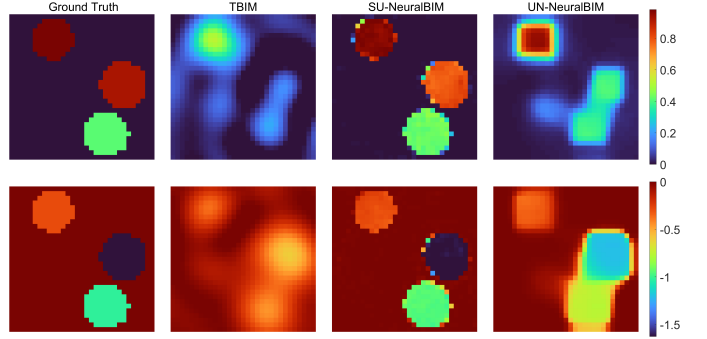


Fig. 22. Comparison between reconstructions of TBIM, supervised NeuralBIM and unsupervised NeuralBIM. From left to right are ground truth, reconstructions of TBIM, supervised NeuralBIM and unsupervised NeuralBIM. The first row shows the real parts and the second shows the imaginary parts.

TABLE IV
PERFORMANCE OF TBIM, SUPERVISED AND UNSUPERVISED NEURAL BIM

	TBIM	SU-NeuralBIM*	UN-NeuralBIM ⁺
Training time	0	$\approx 41h$	$\approx 45h$
Inference time	4.25s	0.046s	0.046s
MAE (Real/Imag)	0.177/0.216	0.0297/0.0280	0.113/0.132

* Supervised NeuralBIM

⁺ Unsupervised NeuralBIM

of both supervised and unsupervised NeuralBIM. Figure 22 illustrates the comparison between reconstructions of TBIM, supervised and unsupervised NeuralBIM. TBIM can locate the positions of three cylinders, but it cannot capture the accurate shapes of scatterers with some artifacts. Supervised NeuralBIM demonstrates the best performance. The inverted result is high-resolution and the difference from the ground truth primarily lies on the boundaries of cylinders. Unsupervised NeuralBIM can also locate the cylinders and provide better shapes of scatterers than TBIM. The detailed comparison of performance is summarized in Table IV. Although supervised and unsupervised NeuralBIM needs approximately 41 hours and 45 hours for offline training respectively, they demonstrates a significant reduction in online computing time compared to TBIM. The MAEs between ground truth and reconstructions of these methods further validate the aforementioned observations derived from Figure 22.

C. Experimental Data Inversion

In this section, we validate unsupervised NeuralBIM with experimental data inversion. The experimental data is published by Institut Fresnel [51]. The TM polarized measured data of *FoamDieInt* and *FoamDieExt* models are selected for inversion. The frequency of measured data is 3 GHz. The measurement is performed with 8 transmitters and 241 receivers in [51]. The measurement configuration is different

TABLE V
TRAINING SETTINGS IN EXPERIMENTAL DATA INVERSION

Cylinder	Radius	Contrast (Real)	Contrast (Imag)
A	0.03-0.045m	0.2-0.8	0
B	0.01-0.02m	1.5-2.3	0

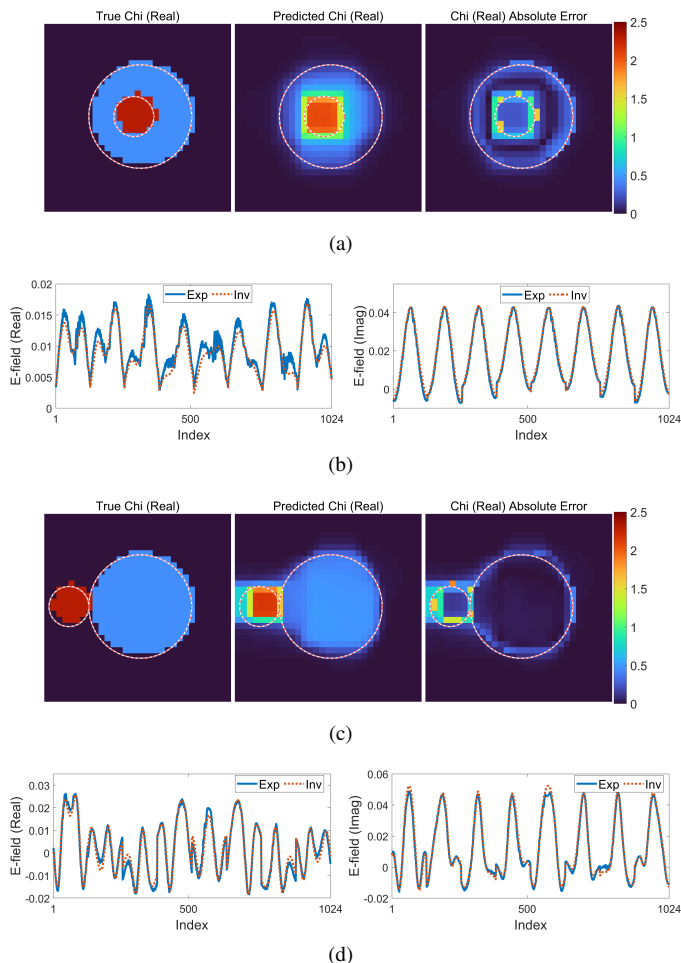


Fig. 23. Experimental data inversion of *FoamDielInt* model [(a), (b)] and *FoamDielExt* model [(c), (d)]. (a) and (c): the ground truth, reconstruction, and their corresponding absolute error distribution. (b) and (d): the inverted (red dashed line) and measured (blue solid line) scattered field.

from the synthetic one. The Green's functions in Eq. (3) and Eq. (4) are changed as a result. Because the Green's functions are incorporated, NeuralBIM needs to be re-trained when the measurement configuration changes.

The training configuration has 8 transmitters and downsamples 241 receivers to 128 receivers. The training data set of 16000 samples is generated by assuming two cylinders are randomly located inside the DoI. Table V summarizes the geometries and material properties of cylinders. The measured data takes the size of 128×8 and they are reshaped into 32×32 for training.

After the training is finished, unsupervised NeuralBIM is employed to invert the measurement data of *FoamDielInt* and *FoamDielExt* models. Figure 23 shows the reconstructions and the corresponding inverted scattered fields. The reconstructed geometries and material properties of scatterers agree well with the ground truth. Then the scattered fields are calculated based on the reconstructed results. The inverted scattered fields also show a good agreement with the measured ones, which further validate unsupervised NeuralBIM.

VI. CONCLUSIONS

In this paper, neural Born iterative method is proposed to solve 2D inverse scattering problems. Inspired by PhiSRL, NeuralBIM emulates the computational process of TBIM by applying CNNs to learn the parametric functions of alternate update rules. Both supervised and unsupervised learning schemes of NeuralBIM are presented in this paper, and they all demonstrate better performance than TBIM. Numerical and experimental results validate the efficacy of the proposed NeuralBIM. The anti-noise capability and generalization ability of NeuralBIM are also verified.

This paper investigate a potential way to incorporate deep learning techniques into traditional computational electromagnetic algorithms. Additionally, the feasibility is also verified that the physics-incorporated deep neural network can be trained via an unsupervised process to perform reliable computations by applying governing equations as its objective function.

REFERENCES

- [1] X. Chen, *Computational methods for electromagnetic inverse scattering*. John Wiley & Sons, 2018.
- [2] M. Salucci, N. Anselmi, G. Oliveri, P. Calmon, R. Miorelli, C. Rebound, and A. Massa, "Real-time NDT-NDE through an innovative adaptive partial least squares SVR inversion approach," *IEEE Transactions on Geoscience and Remote Sensing*, vol. 54, no. 11, pp. 6818–6832, 2016.
- [3] A. Abubakar, P. M. Van den Berg, and J. J. Mallorqui, "Imaging of biomedical data using a multiplicative regularized contrast source inversion method," *IEEE Transactions on Microwave Theory and Techniques*, vol. 50, no. 7, pp. 1761–1771, 2002.
- [4] M. Pastorino and A. Randazzo, *Microwave Imaging Methods and Applications*. Artech House, 2018.
- [5] A. Abubakar, T. Habashy, V. Druskin, L. Knizhnerman, and D. Alumbaugh, "2.5 D forward and inverse modeling for interpreting low-frequency electromagnetic measurements," *Geophysics*, vol. 73, no. 4, pp. F165–F177, 2008.
- [6] M. Salucci, L. Poli, N. Anselmi, and A. Massa, "Multifrequency particle swarm optimization for enhanced multiresolution GPR microwave imaging," *IEEE Transactions on Geoscience and Remote Sensing*, vol. 55, no. 3, pp. 1305–1317, 2016.
- [7] M. Slaney, A. C. Kak, and L. E. Larsen, "Limitations of imaging with first-order diffraction tomography," *IEEE transactions on microwave theory and techniques*, vol. 32, no. 8, pp. 860–874, 1984.
- [8] A. Devaney, "Inverse-scattering theory within the Rytov approximation," *Optics letters*, vol. 6, no. 8, pp. 374–376, 1981.
- [9] K. Belkebir, P. C. Chaumet, and A. Sentenac, "Superresolution in total internal reflection tomography," *JOSA A*, vol. 22, no. 9, pp. 1889–1897, 2005.
- [10] Y. Wang and W. C. Chew, "An iterative solution of the two-dimensional electromagnetic inverse scattering problem," *International Journal of Imaging Systems and Technology*, vol. 1, no. 1, pp. 100–108, 1989.
- [11] W. C. Chew and Y.-M. Wang, "Reconstruction of two-dimensional permittivity distribution using the distorted Born iterative method," *IEEE transactions on medical imaging*, vol. 9, no. 2, pp. 218–225, 1990.
- [12] P. Van den Berg and A. Abubakar, "Contrast source inversion method: State of art," *Progress in Electromagnetics Research*, vol. 34, pp. 189–218, 2001.
- [13] A. Zakaria, C. Gilmore, and J. LoVetri, "Finite-element contrast source inversion method for microwave imaging," *Inverse Problems*, vol. 26, no. 11, p. 115010, 2010.
- [14] X. Chen, "Subspace-based optimization method for solving inverse-scattering problems," *IEEE Transactions on Geoscience and Remote Sensing*, vol. 48, no. 1, pp. 42–49, 2009.
- [15] O. Dorn and D. Lesselier, "Level set methods for inverse scattering," *Inverse Problems*, vol. 22, no. 4, p. R67, 2006.
- [16] P. Mojabi and J. LoVetri, "Overview and classification of some regularization techniques for the Gauss-Newton inversion method applied to inverse scattering problems," *IEEE Transactions on Antennas and Propagation*, vol. 57, no. 9, pp. 2658–2665, 2009.

- [17] G. H. Golub, P. C. Hansen, and D. P. O’Leary, “Tikhonov regularization and total least squares,” *SIAM journal on matrix analysis and applications*, vol. 21, no. 1, pp. 185–194, 1999.
- [18] P. M. van den Berg and R. E. Kleinman, “A total variation enhanced modified gradient algorithm for profile reconstruction,” *Inverse Problems*, vol. 11, no. 3, p. L5, 1995.
- [19] E. J. Candès and M. B. Wakin, “An introduction to compressive sampling,” *IEEE signal processing magazine*, vol. 25, no. 2, pp. 21–30, 2008.
- [20] G. Oliveri, M. Salucci, N. Anselmi, and A. Massa, “Compressive Sensing as Applied to Inverse Problems for Imaging: Theory, applications, current trends, and open challenges,” *IEEE Antennas and Propagation Magazine*, vol. 59, no. 5, pp. 34–46, 2017.
- [21] L. Guo and A. Abbosh, “Microwave stepped frequency head imaging using compressive sensing with limited number of frequency steps,” *IEEE Antennas and Wireless Propagation Letters*, vol. 14, pp. 1133–1136, 2015.
- [22] G. Oliveri, L. Poli, N. Anselmi, M. Salucci, and A. Massa, “Compressive sensing-based Born iterative method for tomographic imaging,” *IEEE Transactions on Microwave Theory and Techniques*, vol. 67, no. 5, pp. 1753–1765, 2019.
- [23] L. Pan, X. Chen, and S. P. Yeo, “A compressive-sensing-based phaseless imaging method for point-like dielectric objects,” *IEEE transactions on antennas and propagation*, vol. 60, no. 11, pp. 5472–5475, 2012.
- [24] L. Guo, M. Li, S. Xu, and F. Yang, “Application of Stochastic Gradient Descent Technique for Method of Moments,” in *2020 IEEE International Conference on Computational Electromagnetics (ICCEM)*. IEEE, 2020, pp. 97–98.
- [25] T. Shan, R. Guo, M. Li, F. Yang, S. Xu, and L. Liang, “Application of Multitask Learning for 2-D Modeling of Magnetotelluric Surveys: TE Case,” *IEEE Transactions on Geoscience and Remote Sensing*, vol. 60, pp. 1–9, 2021.
- [26] T. Shan, W. Tang, X. Dang, M. Li, F. Yang, S. Xu, and J. Wu, “Study on a fast solver for Poisson’s equation based on deep learning technique,” *IEEE Transactions on Antennas and Propagation*, vol. 68, no. 9, pp. 6725–6733, 2020.
- [27] A. Massa, D. Marcantonio, X. Chen, M. Li, and M. Salucci, “DNNs as applied to electromagnetics, antennas, and propagation—A review,” *IEEE Antennas and Wireless Propagation Letters*, vol. 18, no. 11, pp. 2225–2229, 2019.
- [28] T. Shan, X. Pan, M. Li, S. Xu, and F. Yang, “Coding programmable metasurfaces based on deep learning techniques,” *IEEE Journal on Emerging and Selected Topics in Circuits and Systems*, vol. 10, no. 1, pp. 114–125, 2020.
- [29] T. Shan, M. Li, S. Xu, and F. Yang, “Phase Synthesis of Beam-Scanning Reflectarray Antenna Based on Deep Learning Technique,” *Progress In Electromagnetics Research*, vol. 172, pp. 41–49, 2021.
- [30] X. Chen, Z. Wei, M. Li, and P. Rocca, “A review of deep learning approaches for inverse scattering problems (invited review),” *Progress In Electromagnetics Research*, vol. 167, pp. 67–81, 2020.
- [31] M. Salucci, M. Arrebola, T. Shan, and M. Li, “Artificial Intelligence: New Frontiers in Real-Time Inverse Scattering and Electromagnetic Imaging,” *IEEE Transactions on Antennas and Propagation*, 2022.
- [32] R. Guo, X. Song, M. Li, F. Yang, S. Xu, and A. Abubakar, “Supervised descent learning technique for 2-D microwave imaging,” *IEEE Transactions on Antennas and Propagation*, vol. 67, no. 5, pp. 3550–3554, 2019.
- [33] K. Xu, L. Wu, X. Ye, and X. Chen, “Deep learning-based inversion methods for solving inverse scattering problems with phaseless data,” *IEEE Transactions on Antennas and Propagation*, vol. 68, no. 11, pp. 7457–7470, 2020.
- [34] R. Zhang, Q. Sun, Y. Mao, L. Cui, Y. Jia, W.-F. Huang, M. Ahmadian, and Q. H. Liu, “Accelerating Hydraulic Fracture Imaging by Deep Transfer Learning,” *IEEE Transactions on Antennas and Propagation*, 2022.
- [35] R. Song, Y. Huang, K. Xu, X. Ye, C. Li, and X. Chen, “Electromagnetic inverse scattering with perceptual generative adversarial networks,” *IEEE Transactions on Computational Imaging*, vol. 7, pp. 689–699, 2021.
- [36] L. Li, L. G. Wang, F. L. Teixeira, C. Liu, A. Nehorai, and T. J. Cui, “DeepNIS: Deep neural network for nonlinear electromagnetic inverse scattering,” *IEEE Transactions on Antennas and Propagation*, vol. 67, no. 3, pp. 1819–1825, 2018.
- [37] L. Guo, G. Song, and H. Wu, “Complex-Valued Pix2pix—Deep Neural Network for Nonlinear Electromagnetic Inverse Scattering,” *Electronics*, vol. 10, no. 6, p. 752, 2021.
- [38] Z. Wei and X. Chen, “Deep-Learning Schemes for Full-Wave Nonlinear Inverse Scattering Problems,” *IEEE Transactions on Geoscience and Remote Sensing*, 2018.
- [39] G. Chen, P. Shah, J. Stang, and M. Moghaddam, “Learning-assisted multimodality dielectric imaging,” *IEEE Transactions on Antennas and Propagation*, vol. 68, no. 3, pp. 2356–2369, 2019.
- [40] Y. Sanghvi *et al.*, “Embedding deep learning in inverse scattering problems,” *IEEE Transactions on Computational Imaging*, vol. 6, pp. 46–56, 2019.
- [41] Y. Lu, A. Zhong, Q. Li, and B. Dong, “Beyond finite layer neural networks: Bridging deep architectures and numerical differential equations,” in *International Conference on Machine Learning*. PMLR, 2018, pp. 3276–3285.
- [42] E. Haber and L. Ruthotto, “Stable architectures for deep neural networks,” *Inverse problems*, vol. 34, no. 1, p. 014004, 2017.
- [43] E. Weinan, “A proposal on machine learning via dynamical systems,” *Communications in Mathematics and Statistics*, vol. 5, no. 1, pp. 1–11, 2017.
- [44] T. Shan, X. Song, R. Guo, M. Li, F. Yang, and S. Xu, “Physics-informed Supervised Residual Learning for Electromagnetic Modeling,” in *2021 International Applied Computational Electromagnetics Society Symposium (ACES)*. IEEE, 2021, pp. 1–4.
- [45] L. Xiao, Y. Bahri, J. Sohl-Dickstein, S. S. Schoenholz, and J. Pennington, “Dynamical Isometry and a Mean Field Theory of CNNs: How to Train 10,000-Layer Vanilla Convolutional Neural Networks,” Jul. 2018.
- [46] W. Tarnowski, P. Warchol, S. Jastrzebski, J. Tabor, and M. Nowak, “Dynamical isometry is achieved in residual networks in a universal way for any activation function,” in *The 22nd International Conference on Artificial Intelligence and Statistics*. PMLR, 2019.
- [47] Z. Long, Y. Lu, X. Ma, and B. Dong, “Pde-net: Learning pdes from data,” in *International Conference on Machine Learning*. PMLR, 2018, pp. 3208–3216.
- [48] L. Ruthotto and E. Haber, “Deep neural networks motivated by partial differential equations,” *Journal of Mathematical Imaging and Vision*, vol. 62, no. 3, pp. 352–364, 2020.
- [49] K. He, X. Zhang, S. Ren, and J. Sun, “Deep residual learning for image recognition,” in *Proceedings of the IEEE conference on computer vision and pattern recognition*, 2016, pp. 770–778.
- [50] D.-A. Clevert, T. Unterthiner, and S. Hochreiter, “Fast and accurate deep network learning by exponential linear units (elus),” *arXiv preprint arXiv:1511.07289*, 2015.
- [51] J.-M. Geffrin, P. Sabouroux, and C. Eyraud, “Free space experimental scattering database continuation: experimental set-up and measurement precision,” *inverse Problems*, vol. 21, no. 6, p. S117, 2005.